PAPER

Check for updates

Boosting solid oxide fuel cell performance *via* electrolyte thickness reduction and cathode infiltration†

Beom-Kyeong Park [ID] and Scott A. Barnett [ID] *

Increasing the power density and reducing the operating temperature of solid oxide fuel cells (SOFCs) is important for improving commercial viability. Here we discuss two strategies for achieving such improvements in Ni–YSZ supported SOFCs – electrolyte thickness reduction and cathode infiltration. Microstructural and electrochemical results are presented showing the effect of reducing YSZ/GDC electrolyte thickness from 8 to 2.5 μm, and the effect of PrO_x infiltration into the LSCF–GDC cathode. Both of these measures are effective, particularly at lower temperatures, leading to an increase in the maximum power density at 650 °C from 0.4 to 0.95 W cm^{-2}, for example. Electrochemical impedance spectroscopy utilizing subtractive analysis shows that PrO_x enhances the cathode charge transfer process. Reducing the electrolyte thickness reduces not only the cell ohmic resistance but also the electrode polarization resistance. The latter effect appears to be an artifact associated with a slight increase in the steam partial pressure at the anode due to minor gas leakage across the thinner electrolyte.

1. Introduction

The solid oxide fuel cell (SOFC) is an environmentally-benign device that produces electricity with high energy conversion efficiency through an electrochemical reaction between chemical fuels (*e.g.*, H_2, CH_4) and air at high temperatures (600–800 °C).[1–3] SOFCs can provide continuous or on-demand power, while devices similar to SOFCs can be operated reversibly for converting renewable electricity to fuel.[1,4–6] Thus, the technology can provide an important complement intermittent renewable energy sources such as solar and wind power.[1,2,7]

There has been considerable emphasis on increasing SOFC power density to reduce stack size and cost, and reducing operating temperature to allow broader materials selection and reduced cost for both the stack and balance of plant, lower cell degradation, and more rapid start-up.[2,8–12] Ni–Y_2O_3-doped ZrO_2 (YSZ) anode-supported cells (ASCs) with thin (~10 μm) YSZ electrolytes typically provide the highest power density along with reasonable operating temperature, down to ~700 °C. In order to improve upon these, alternative materials are utilized along with alternative processing methods. In order to reduce electrolyte ohmic resistance, alternative materials including Gd_2O_3-doped CeO_2 (GDC) and strontium-/magnesium-doped lanthanum gallate (LSGM) are utilized,[12–15] but the mixed conductivity of GDC under a reducing atmosphere and the

materials incompatibility of LSGM are significant issues.[14–16] Alternatively, the thickness of the conventional YSZ electrolyte can be reduced.[8,11,17–19] There are numerous examples of cells with YSZ electrolyte thickness of ~1 μm.[18,20,21] For example, Oh *et. al.* reported ~1.02 W cm^{-2} at 600 °C for the ~0.5 μm-thick YSZ/GDC bi-layer electrolyte cell fabricated *via* the chemical solution deposition.[8] However, these reports have generally used novel processing methods such as PLD,[18] sputtering,[21] or sol–gel[20] for thin-electrolyte fabrication.

It is well known that cathode polarization resistance is an important limitation on SOFC power density, especially at lower temperature. A range of new cathode materials have been tested, often yielding very good performance.[2,3,22] One important approach is the introduction of catalytic nanoparticles, typically using wet-chemical infiltration, *e.g.*, an MIEC such as $Sm_{0.5}Sr_{0.5}CoO_3$ (SSC) into an ionic conductor scaffold such as GDC[23] or a MIEC scaffold such as LSCF.[24] Recently, PrO_x infiltration has been shown to provide very good low-temperature cathode performance when infiltrated into GDC[25] or MIEC cathode scaffolds.[26] However, neither the electrochemical characteristics of PrO_x-infiltrated LSCF–GDC cathodes nor their full-cell performance has been reported.

Here we report on the electrochemical performance of Ni–YSZ-supported cells GDC/YSZ bi-layer electrolyte thickness reduced from a typical value of 8 to 2.5 μm. Unlike prior work with such thin electrolytes, the YSZ electrolyte and Ni–YSZ layers were fabricated using a standard tape casting and co-firing approach. In addition, new results are reported on electrochemical response changes and full cell performance improvement resulting from PrO_x infiltration into composite

Department of Materials Science and Engineering, Northwestern University, Evanston, Illinois 60208, USA. E-mail: s-barnett@northwestern.edu

$La_{0.6}Sr_{0.4}Co_{0.2}Fe_{0.8}O_3$ (LSCF)–GDC cathodes. The resultant ASCs were electrochemically characterized at different temperatures and fuel compositions. To gain fundamental insights into the factors affecting the cell performance, a unique impedance subtraction method is utilized to identify the changes in contributions of all reactions for full cells. The ∼2.5 μm-thick YSZ/GDC bi-layer electrolyte SOFC yields the high maximum power density of ∼2.38 W cm^{-2} at 800 °C, but can also provide good low-temperature performance, e.g., ∼0.95 W cm^{-2} at 650 °C.

2. Results and discussion

Fig. 1(a)–(c) show SEM images taken after cell electrochemical testing was completed (∼6 h and 600–800 °C) for the three cell types – the baseline cell with 8 μm thick electrolyte (termed the "t8 cell"), the cell with 2.5 μm thick electrolyte (termed the "t2.5 cell"), and the cell with 2.5 μm thick electrolyte and PrO$_x$ infiltrated cathode (termed the "t2.5Pr cell"). The electrolytes are reasonably dense with small isolated pores. The electrode/electrolyte interfaces are well connected without voids or delamination. The Ni–YSZ anode and LSCF–GDC cathode functional layers show the expected porous microstructures. The insets in (b) and (c) show higher magnification views of the LSCF–GDC cathodes; in (c), the porous microstructure is decorated with nanoparticles, presumably PrO$_x$, that are not present in (b). An SEM-EDS analysis (Fig. S1†) yields an estimate of the electrolyte thicknesses – ∼1.5 μm for YSZ in the t2.5 cell and ∼7 μm for YSZ in the t8 cell, and ∼1 μm for GDC in both cells – and an estimated YSZ/GDC interface width of ∼0.5 μm in both cells, low enough to minimize the electrolyte resistance contribution from the low-conductivity intermixed layer.[27]

Fig. 2(a)–(c) compare the voltage and power density versus current density measured at 600, 700, and 800 °C in 3 vol% H_2O-humidified H_2 and air for the three cell types (see Fig. S2† for all the j–V temperature dependent data). All of the cells show the expected increase in current density and power density with increasing temperature. The j–V dependence shows a slightly positive curvature, indicating that electrode activation polarization is important. There is also an indication of negative curvature at the highest current densities for the t2.5 and t2.5Pr cells, indicating some concentration polarization. Fig. 2(d) summarizes the maximum power densities (P_{max}) of the three cell types, showing the general increase of P_{max}, e.g., at 700 °C from 0.7 W cm^{-2} for the t8 cell to 1.2 W cm^{-2} for the t2.5 cell to 1.47 W cm^{-2} for the t2.5Pr cell. The percentage increases in P_{max} from t8 to t2.5Pr were generally larger at lower temperature, increasing from 74% at 800 °C to 136% at 600 °C.

Fig. 3(a) compares Nyquist plots of the impedance spectra for the three cell types at 600, 700, and 800 °C. Fig. 3(b) and (c) show the temperature dependences of the ohmic resistance (R_Ω), estimated from the high-frequency real-axis intercepts of the impedance spectra, and the electrode polarization resistance (R_p), estimated from the difference between the high and low frequency real axis intercepts. As expected, R_Ω is lower for the smaller t, especially at lower temperatures. The measured R_Ω values here are close to the values expected given the YSZ, GDC, and interdiffusion layer thicknesses and their respective conductivities; for example, at 800 °C, the measured R_Ω value of ∼0.05 Ω cm^2 was found to match with the value (∼0.04 Ω cm^2)

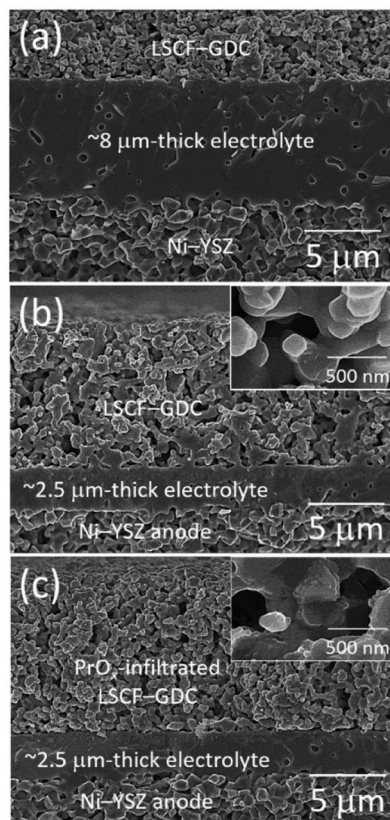**Fig. 1** Fracture cross-sectional SEM images of (a) the baseline cell with 8 μm thick electrolyte ("t8 cell"); (b) LSCF–GDC cathode ("t2.5 cell") and (c) the cell with reduced (2.5 μm) electrolyte thickness and PrO$_x$-infiltrated LSCF–GDC cathode ("t2.5Pr cell").

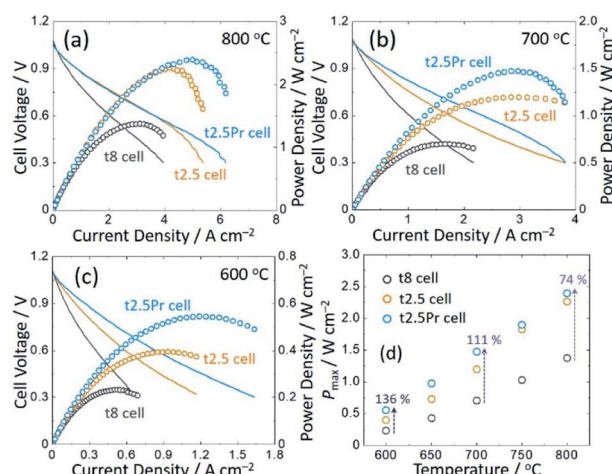**Fig. 2** Comparison plots of voltage and power density versus current density for the t8, t2.5, and t2.5Pr cells measured at (a) 800, (b) 700, and (c) 600 °C in 3 vol% H_2O-humidified H_2 and air. (d) shows a comparison of maximum power densities (P_{max}) for the cells shown in Fig. S1.†
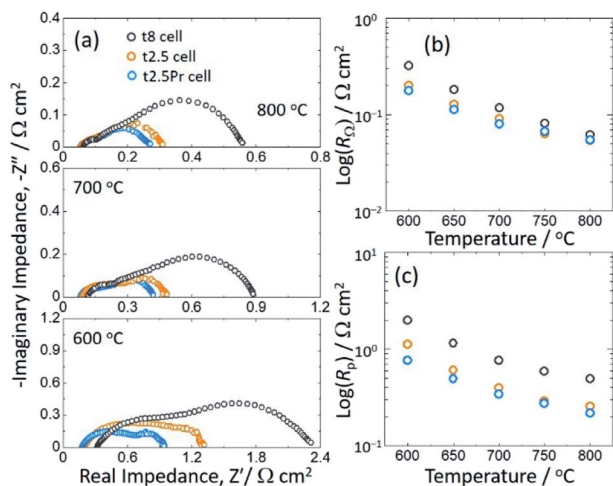
Fig. 3 (a) Nyquist plots of the impedance spectra for the t8, t2.5, and t2.5Pr cells measured at 600, 700, and 800 °C in 3 vol% H_2O-humidified H_2 and air. (b) Ohmic (R_Ω) and (c) electrode polarization resistance (R_p) as a function of temperature for the cells shown in (a).

Fig. 4 The OCV values of the t8 and t2.5 cells for different bubbler humidity values. Note that OCV values are ~30 mV lower than predicted using Nernst equation based on bubbler humidity; this is sometimes observed in button cell tests, presumably because slight gas leakage at the seals yields higher steam content at the cell than in the bubbler.[37]

calculated using ionic conductivities of ~3.08×10^{-2} S cm^{-1} for YSZ,[28] and ~5.60×10^{-2} S cm^{-1} for GDC,[29] and ~1.25×10^{-3} S cm^{-1} for the interdiffusion layer[30] and the thicknesses given above. Based on a decrease in YSZ thickness from 7 to 1.5 μm, the predicted decrease in R_Ω (0.16, 0.044, and 0.018 Ω cm^2 at 600, 700, and 800 °C, respectively) is in reasonable agreement with the decrease shown in Fig. 3 (0.121, 0.028, and 0.009 Ω cm^2 at 600, 700, and 800 °C, respectively).

PrO$_x$ infiltration also yields a decrease in R_p, particularly at lower temperature. The decreases are in reasonable agreement with a prior study of PrO$_x$ infiltration into LSCF in symmetric cells.[26] For example, R_p at 600 °C was observed to decrease by ~0.5 Ω cm^2 with PrO$_x$ infiltration in Fig. 3, similar to that observed previously. This shows that the effect of PrO$_x$ infiltration, which was done using the same methodology in both cases, is similar for different electrode scaffolds – LSCF in the prior work and LSCF–GDC in the present case. Also worthy of mention is the reduced impedance resistance at the low frequency (<1 Hz). This is associated with the improved dissociative adsorption by PrO$_x$,[26] in turn contributing to the reduced concentration polarization as shown in Fig. 2(a). The slight decrease in R_Ω with PrO$_x$ infiltration may be explained by sample-to-sample variations, although there have been reports that electrically conductive infiltrants can reduce R_Ω through the improved connectivity between the active and inactive phases.[31–33]

One surprising result in Fig. 3(c) is the substantial reduction in R_p caused by decreasing t. One possible explanation is a change in the gas compositions due to electrolyte leakage. Evidence of this is given in Fig. 4, which shows the OCV values of the t2.5 cell are ~30 mV lower than for the t8 cell over a range of temperatures. Since a very thin electrolyte with a substantial portion of GDC might be expected to exhibit some electronic leakage, we calculated the leakage current using an electrolyte transport model.[34] However, the calculated leakage current was relatively low for the t2.5 cell, 2.5 mA cm^{-2}, suggesting
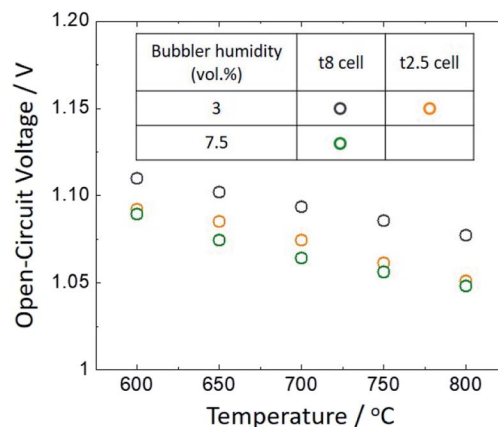
a decrease in OCV of only ~1 mV. Another possibility is that the thinner electrolyte was not completely gas tight, allowing gas leakage; oxygen leakage into the fuel side would generate additional steam, decreasing the OCV. Since the R_p value for Ni–YSZ anodes has been shown to decrease rapidly with increasing steam content,[35,36] small gas leakage could result in a substantial decrease in R_p. Using the Nernst equation (see ESI for details†), the fuel steam content should increase by ~4.5% to yield the 20 mV lower OCV for the t2.5 cell. Thus, a t8 cell was tested with the water bubbler temperature increased to yield this steam content increase, and the OCV value did indeed match that of the t2.5 cell in 3 vol% H_2O (Fig. 4). Fig. 5 compares the impedance spectra at 600, 700 and 800 °C for the t8 cell for different bubbler humidity values, showing that R_p is reduced by increasing the bubbler humidity to 7.5 vol% H_2O, but is still not quite as low as the t2.5 cell. Fig. S3† shows that the P_{max} values of the t8 cell with 7.5 vol% H_2O were substantially higher, e.g., 1.03 W cm^{-2} at 700 °C versus 0.7 W cm^{-2} for 3 vol% H_2O. These results appear to confirm the hypothesis that the lower R_p for the t2.5 cell was due to gas leakage.

In order to better understand the effects of electrolyte thickness and PrO$_x$ infiltration, a detailed analysis of the EIS data is carried out. Although distribution of relaxation time (DRT) analysis is useful to characterize cell processes, it is typically challenging to fully deconvolute the multiple electrochemical responses of a full SOFC that are often overlapped. This is illustrated in Fig. S4† that shows the DRT analysis of the present t8 cell. Thus, we have applied the impedance subtraction method, previously reported by Jensen et al. and Park et. al.,[19,38] to help separate and identify the affected electrochemical processes. Fig. 6 presents the difference $\left(\Delta \dot{Z}' = \Delta \dfrac{\partial Z'(f)}{\partial \ln(f)} \right)$ of real impedance differentiated with respect to $\ln(f)$, where f is the frequency – positive change means a reduction in the impedance.[38] The spectrum S_t,

11628 | J. Mater. Chem. A, 2020, 8, 11626–11631

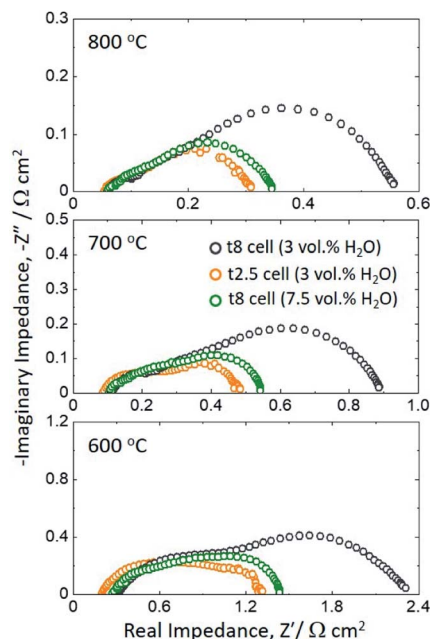This journal is © The Royal Society of Chemistry 2020

Fig. 5 Comparison of impedance spectra in Nyquist plots at 600, 700, and 800 °C for the t8 cells and the t2.5 cell. The cells were tested with bubbler humidities of 3 or 7.5 vol% H_2O.

obtained from the difference between the t8 and t2.5 cells tested in 3% steam, shows that decreasing t reduces the responses at $\sim 10^3$ and ~ 10 Hz. A similar change is seen for S_{steam}, the difference between the 3% and 7.5% steam measurements of the t8 cell. These changes are in good
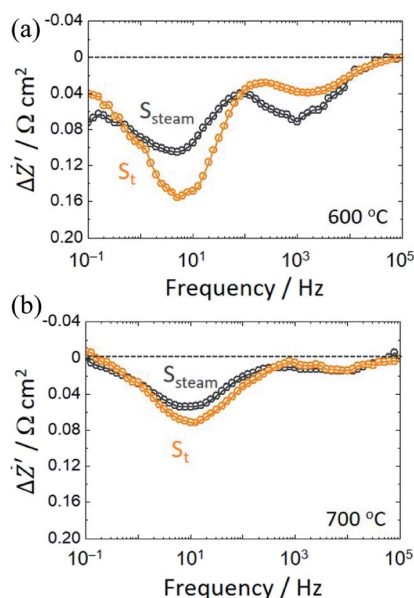

Fig. 6 Impedance difference ($\Delta Z'$) spectra at 600 °C (a) and 700 °C (b). S_{steam} shows the changes caused by increasing the steam content from 3 to 7.5 vol% for the t8 cell. S_t shows the changes from reducing the electrolyte thickness from 8 μm (t8 cell) to ~2.5 μm (t2.5 cell). See Fig. S5† for the other temperatures.
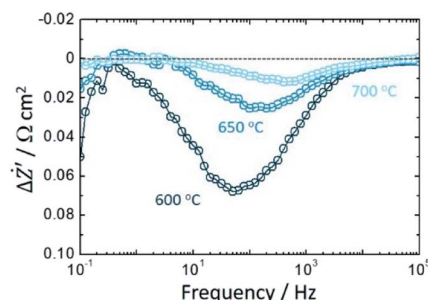

Fig. 7 $\Delta Z'$ spectra obtained from the difference of the EIS data from the t2.5 and t2.5Pr cells, showing the changes caused by PrO_x infiltration into the LSCF−GDC cathode.

agreement with the response changes previously reported for Ni−YSZ anodes due to steam content changes.[35,36,39,40] This strongly supports the conclusion that the R_p reduction caused by reducing electrolyte thickness is mainly due to increased steam at the Ni−YSZ due to electrolyte leakage. Note that gas leakage across the electrolyte also implies the production of a small amount of steam on the air side of the cell. The effect of steam on LSCF is generally an increase in R_p,[41–44] and so this may explain the discrepancy between the R_p values of t8 cell in 7.5% steam and t2.5 cell in 3% steam.

Fig. 7 shows $\Delta Z'$ spectra obtained by subtraction of the t2.5 cell response from the t2.5Pr cell response; at each temperature, the effect of PrO_x infiltration is to reduce the response over a fairly broad frequency range centered at $\sim$50 Hz at 600 °C and $\sim$500 Hz at 700 °C. This is consistent with the data recently reported by Lu *et al.*[26] for PrO_x infiltrated into LSCF, where the response centered at $\sim$50 Hz (at 650 °C) was reduced by the infiltration. As noted above, the magnitude of the response is also similar to that reported in ref. 26.

3. Conclusions

The present results show that both electrolyte thickness reduction and cathode infiltration boost the electrochemical performance of the Ni−YSZ supported cells. The analysis of electrochemical impedance spectroscopy data provides insights into the full cell electrochemical reactions. The main findings are as follows:

(1) The maximum power density at 800 °C was increased from 1.4 to 2.38 W cm^{-2}.

(2) The maximum power density at 650 °C was increased from 0.4 to 0.95 W cm^{-2}, showing the general trend that the performance improvement is more pronounced, on a percentage basis, at lower temperatures.

(3) The electrolyte thickness reduction results in not only reduced R_Ω but also reduced R_p that is mainly due to a few percent increased steam content in the Ni−YSZ by the gas leakage through the thin electrolyte. This strong dependence of the Ni−YSZ R_p value on steam content yielded $\sim$50% of the cell performance improvements.

(4) The PrO_x infiltrant effectively facilitates the charge transfer process of LSCF.

This journal is © The Royal Society of Chemistry 2020

J. Mater. Chem. A, 2020, **8**, 11626–11631 | **11629**

4. Experimental

4.1 Cell fabrication

The commercial LSCF (Praxair) and GDC (Fuelcellmaterials) (50 : 50 in weight) powders were mixed with vehicle (V-737, Heraeus) in a weight ratio of 1 : 1.2 in a three-roll mill to prepare the screen-printing paste. The NiO–YSZ-supported half-cells were produced by tape casting and lamination using 45 wt% NiO–45 wt% YSZ–10 wt% starch (as a support), 50 wt% NiO–50 wt% YSZ (as an electrode functional layer), and YSZ with 1 mol% Fe_2O_3 sintering aid (as an electrolyte). For the tape casting, the blade gap was carefully controlled to obtain the desired YSZ layer thicknesses. After pre-sintering the laminates at 1150 °C for 2 h, the 3 mol% Fe_2O_3-doped GDC layers were deposited on the YSZ surfaces through dip-coating where a slurry was composed of Fe_2O_3 and GDC powders, xylene and isopropyl alcohol as solvents, fish oil as dispersant, and polyvinyl butyral as binder,[45] followed by co-sintering at 1250 °C for 4 h. Note that the Fe_2O_3 (Alfa Aesar, 99.8%) was used as a sintering aid in both the YSZ (1 wt%) and GDC (3 wt%) to achieve high density at the firing temperature of 1250 °C,[27] lower than typically used for sintering YSZ. This measure aimed to reduce the deleterious interdiffusion between YSZ and GDC that occurs during do-firing at higher temperatures.[27] The LSCF–GDC cathode (active area: 0.5 cm^2) was screen-printed onto the GDC diffusion barrier layer of the half-cell and then fired at 1100 °C for 2 h in air to yield a 10 μm thick electrode.

4.2 PrO$_x$ infiltration

A PrO$_x$ precursor solution was prepared by dissolving 1 mol L^{-1} Pr(NO$_3$)$_3$·6H$_2$O in distilled water. 2 wt% Triton X-100 surfactant and 2 mol L^{-1} citric acid chelating agent were added into the precursor solution. The LSCF–GDC cathodes were infiltrated in a single step with 2 μL of PrO$_x$ solution. The deposit was calcined during the initial heating of the SOFC to its operating temperature, resulting in the formation of PrO$_x$ nanoparticles.[26]

4.3 Electrochemical characterization

For the full cell testing, gold grids (Heraeus) were screen-printed on the cathodes for current collection. The cells were mounted and sealed onto alumina tubes using silver paste (DAD-87, Shanghai Research Institute of Synthetic Resins). During the fuel cell testing, the cathode was fed with ambient air and the anode was fed with H_2 that was humidified by bubbling through a H_2O bath kept at different temperatures to adjust humidification level. The electrochemical characterization was carried out with an IM6 Electrochemical Workstation (ZAHNER) at 600–800 °C. The EIS data were collected under open circuit conditions by using a 20 mV ac signal in the frequency range of from 0.1 Hz to 100 kHz.

4.4 Materials characterization

Microstructural and compositional measurements were performed on the post-test cells using scanning electron microscopy (SEM, Hitachi S-4800) combined with energy-dispersive X-ray spectroscopy (EDS, Oxford INCA).

Conflicts of interest

There are no conflicts to declare.

Acknowledgements

References

1 C. Graves, S. D. Ebbesen, S. H. Jensen, S. B. Simonsen and M. B. Mogensen, *Nat. Mater.*, 2014, **14**, 239–244.

2 Z. Gao, L. V. Mogni, E. C. Miller, J. G. Railsback and S. A. Barnett, *Energy Environ. Sci.*, 2016, **9**, 1602–1644.

3 S.-L. Zhang, H. Wang, M. Y. Lu, A.-P. Zhang, L. V. Mogni, Q. Liu, C.-X. Li, C.-J. Li and S. A. Barnett, *Energy Environ. Sci.*, 2018, **11**, 1870–1879.

4 S. H. Jensen, C. Graves, M. Mogensen, C. Wendel, R. Braun, G. Hughes, Z. Gao and S. A. Barnett, *Energy Environ. Sci.*, 2015, **8**, 2471–2479.

5 C. H. Wendel, Z. Gao, S. A. Barnett and R. J. Braun, *J. Power Sources*, 2015, **283**, 329–342.

6 D. M. Bierschenk, J. R. Wilson and S. A. Barnett, *Energy Environ. Sci.*, 2011, **4**, 944–951.

7 B.-K. Park, Q. Zhang, P. W. Voorhees and S. A. Barnett, *Energy Environ. Sci.*, 2019, **12**, 3053–3062.

8 E.-O. Oh, C.-M. Whang, Y.-R. Lee, S.-Y. Park, D. H. Prasad, K. J. Yoon, J.-W. Son, J.-H. Lee and H.-W. Lee, *Adv. Mater.*, 2012, **24**, 3373–3377.

9 B.-K. Park, S.-B. Lee, T.-H. Lim, R.-H. Song and J.-W. Lee, *ChemSusChem*, 2018, **11**, 2620–2627.

10 D. Ding, X. Li, S. Y. Lai, K. Gerdes and M. Liu, *Energy Environ. Sci.*, 2014, **7**, 552–575.

11 B. Shri Prakash, R. Pavitra, S. Senthil Kumar and S. T. Aruna, *J. Power Sources*, 2018, **381**, 136–155.

12 Z. Gao, E. C. Miller and S. A. Barnett, *Adv. Funct. Mater.*, 2014, **24**, 5703–5709.

13 C. Kim, J. Kim, J. Shin and G. Kim, *Int. J. Hydrogen Energy*, 2014, **39**, 20812–20818.

14 E. D. Wachsman and K. T. Lee, *Science*, 2011, **334**, 935–939.

15 Z. Zhan, D. M. Bierschenk, J. S. Cronin and S. A. Barnett, *Energy Environ. Sci.*, 2011, **4**, 3951–3954.

16 Y. Lin and S. A. Barnett, *Electrochem. Solid-State Lett.*, 2006, **9**, A285–A288.

17 T. Tsai, E. Perry and S. Barnett, *J. Electrochem. Soc.*, 1997, **144**, L130–L132.

18 D.-H. Myung, J. Hong, K. Yoon, B.-K. Kim, H.-W. Lee, J.-H. Lee and J.-W. Son, *J. Power Sources*, 2012, **206**, 91–96.

11630 | *J. Mater. Chem. A*, 2020, **8**, 11626–11631

This journal is © The Royal Society of Chemistry 2020

19 B.-K. Park, R. Scipioni, Q. Zhang, D. Cox, P. W. Voorhees and S. A. Barnett, *J. Mater. Chem. A*, 2020, DOI: 10.1039/D0TA04555A.

20 F. Han, R. Mücke, T. Van Gestel, A. Leonide, N. H. Menzler, H. P. Buchkremer and D. Stöver, *J. Power Sources*, 2012, **218**, 157–162.

21 R. Nédélec, S. Uhlenbruck, D. Sebold, V. A. C. Haanappel, H. P. Buchkremer and D. Stöver, *J. Power Sources*, 2012, **205**, 157–163.

22 Z. Shao and S. M. Haile, *Nature*, 2004, **431**, 170–173.

23 A. V. Call, J. G. Railsback, H. Q. Wang and S. A. Barnett, *Phys. Chem. Chem. Phys.*, 2016, **18**, 13216–13222.

24 K. J. Yoon, M. Biswas, H.-J. Kim, M. Park, J. Hong, H. Kim, J.-W. Son, J.-H. Lee, B.-K. Kim and H.-W. Lee, *Nano Energy*, 2017, **36**, 9–20.

25 C. Nicollet, A. Flura, V. Vibhu, A. Rougier, J.-M. Bassat and J.-C. Grenier, *Int. J. Hydrogen Energy*, 2016, **41**, 15538–15544.

26 M. Y. Lu, R. Scipioni, B.-K. Park, T. Yang, Y. A. Chart and S. A. Barnett, *Mater. Today Energy*, 2019, **14**, 100362.

27 Z. Gao, V. Y. Zenou, D. Kennouche, L. Marks and S. A. Barnett, *J. Mater. Chem. A*, 2015, **3**, 9955–9964.

28 W. G. Coors, J. R. O'Brien and J. T. White, *Solid State Ionics*, 2009, **180**, 246–251.

29 V. V. Kharton, F. M. Figueiredo, L. Navarro, E. N. Naumovich, A. V. Kovalevsky, A. A. Yaremchenko, A. P. Viskup, A. Carneiro, F. M. B. Marques and J. R. Frade, *J. Mater. Sci.*, 2001, **36**, 1105–1117.

30 A. Tsoga, A. Gupta, A. Naoumidis and P. Nikolopoulos, *Acta Mater.*, 2000, **48**, 4709–4714.

31 S. Lee, N. Miller, M. Staruch, K. Gerdes, M. Jain and A. Manivannan, *Electrochim. Acta*, 2011, **56**, 9904–9909.

32 Y. Chen, J. Bunch, C. Jin, C. Yang and F. Chen, *J. Power Sources*, 2012, **204**, 40–45.

33 X. Zhang, L. Liu, Z. Zhao, L. Shang, B. Tu, D. Ou, D. Cui and M. Cheng, *Int. J. Hydrogen Energy*, 2015, **40**, 3332–3337.

34 Q. Zhang, Q. Liu, S. A. Barnett and P. W. Voorhees, 2020, submitted.

35 B.-K. Park, R. Scipioni, D. Cox and S. A. Barnett, *J. Mater. Chem. A*, 2020, **8**, 4099–4106.

36 W. Pan, K. Chen, N. Ai, Z. Lü and S. P. Jiang, *J. Electrochem. Soc.*, 2016, **163**, F106–F114.

37 H. Xu, B. Chen, P. Tan, J. Xuan, M. M. Maroto-Valer, D. Farrusseng, Q. Sun and M. Ni, *Appl. Energy*, 2019, **235**, 602–611.

38 S. H. Jensen, A. Hauch, P. V. Hendriksen, M. Mogensen, N. Bonanos and T. Jacobsen, *J. Electrochem. Soc.*, 2007, **154**, B1325–B1330.

39 T. Ramos, M. Søgaard and M. B. Mogensen, *J. Electrochem. Soc.*, 2014, **161**, F434–F444.

40 H. P. Dasari, S.-Y. Park, J. Kim, J.-H. Lee, B.-K. Kim, H.-J. Je, H.-W. Lee and K. J. Yoon, *J. Power Sources*, 2013, **240**, 721–728.

41 R. R. Liu, S. H. Kim, S. Taniguchi, T. Oshima, Y. Shiratori, K. Ito and K. Sasaki, *J. Power Sources*, 2011, **196**, 7090–7096.

42 Y. L. Huang, C. Pellegrinelli and E. D. Wachsman, *J. Electrochem. Soc.*, 2016, **163**, F171–F182.

43 A. Esquirol, N. P. Brandon, J. A. Kilner and M. Mogensen, *J. Electrochem. Soc.*, 2004, **151**, A1847–A1855.

44 J. Wang, Z. Yang, X. He, Y. Chen, Z. Lei and S. Peng, *Int. J. Hydrogen Energy*, 2019, **44**, 3055–3062.

45 S. D. Kim, S. H. Hyun, J. Moon, J.-H. Kim and R. H. Song, *J. Power Sources*, 2005, **139**, 67–72.

This journal is © The Royal Society of Chemistry 2020

J. Mater. Chem. A, 2020, **8**, 11626–11631 | **11631**